Enhanced Energy Storage Performance and Efficiency in Bi0.5(Na0.8K0.2)0.5TiO3–Bi0.2Sr0.7TiO3 Relaxor Ferroelectric Ceramics via Domain Engineering

Srinivas Pattipaka , Hyunsu Choi , Yeseul Lim , Kwi-Il Park , Kyeongwoon Chung , And Geon Tae Hwang *

Posted Date: 8 June 2023

doi: 10.20944/preprints202306.0591.v1

Keywords: Lead-free ceramic capacitors; Dielectric; Relaxor ferroelectric; Domain engineering; Energy storage

Article

Enhanced Energy Storage Performance and Efficiency in $Bi_{0.5}(Na_{0.8}K_{0.2})_{0.5}TiO_3$–$Bi_{0.2}Sr_{0.7}TiO_3$ Relaxor Ferroelectric Ceramics via Domain Engineering

Srinivas Pattipaka [1], Hyunsu Choi [1], Yeseul Lim [1], Kwi-Il Park [2], Kyeongwoon Chung [3] and Geon Tae Hwang [1,*]

[1] Department of Materials Science and Engineering, Pukyong National University, 45, Yongso-ro, Nam-Gu, Busan 48513, Republic of Korea.
[2] School of Materials Science and Engineering, Kyungpook National University, 80 Daehak-ro, Buk-gu, Daegu 41566, Republic of Korea.
[3] Department of Biofibers and Biomaterials Science, Kyungpook National University, Daegu, 41566, Republic of Korea.
* Correspondence: gthwang@pknu.ac.kr

Abstract: In this work, we report the electric energy storage properties of (1-x) $Bi_{0.5}(Na_{0.8}K_{0.2})_{0.5}TiO_3$ – x $Bi_{0.2}Sr_{0.7}TiO_3$ (BNKT-BST; x = 0.15-0.50) relaxor ferroelectric ceramics enhanced via a domain engineering method. A rhombohedral–tetragonal phase, the formation of highly dynamic PNRs, and a dense microstructure are confirmed from XRD, Raman vibrational spectra, and microscopic investigations. The relative dielectric permittivity (2664 at 1 kHz) and loss factor (0.058) were gradually improved with BST (x=0.45). The incorporation of BST into BNKT can disturb the long-range ferroelectric order, lowering the dielectric maximum temperature T_m and inducing the formation of highly dynamic polar nano-regions. In addition, the T_m shifts toward high temperature with frequency and a diffuse phase transition, indicating relaxor ferroelectric characteristics of BNKT-BST ceramics, which is confirmed by the modified Curie Weiss law (γ=1.83). The rhombohedral–tetragonal phase, fine grain size, and lowered T_m with relaxor properties synergistically contribute to a high recoverable energy density W_{rec} of 0.81 J/cm^3 and a high energy efficiency η of 86.95% at 90 kV/cm for x = 0.45.

Keywords: lead-free ceramic capacitors; dielectric; relaxor ferroelectric; domain engineering; energy storage

1. Introduction

Materials with high energy and power have received extensive attention for high-power applications, such as microwaves, electromagnetic devices, pulsed power devices, hybrid electric vehicles, high-frequency inverters, and other energy storage devices [1–3]. In particular, dielectric ceramics are the most promising materials for energy storage applications owing to their super-fast charge-discharge rate and excellent temperature stability as compared to electrochemical energy storage devices (batteries and electrochemical capacitors) and dielectric polymers [4–6]. However, the dielectric capacitor's energy storage density and energy efficiency are much lower than those of polymers/batteries due to their low dielectric breakdown strength (DBS), which restricts their practical application in energy storage devices.

The recoverable energy density (W_{rec}) of a dielectric capacitor is governed by the applied electric field (E) and induced polarization (P), expressed by the following equation, usually estimated from the P–E loop, and is schematically shown in Figure 1a by shaded area with cyan color [7–9].

$$W_{rec} = \int_{P_r}^{P_{max}} E \, dP \qquad (1)$$

Preprints (www.preprints.org) | NOT PEER-REVIEWED | Posted: 8 June 2023 doi:10.20944/preprints202306.0591.v1

where P_{max} and P_r are the maximum polarization and remnant polarization, respectively (Figure 1a). Among all dielectrics, the relaxor ferroelectric (RFE) and antiferroelectric (AFE) materials with a perovskite structure are suitable candidates for energy storage applications since they possess a large P_{max}, small P_r, and slim P-E loops at higher fields. This leads to high energy efficiency (η), which can be estimated by the following equation. [8,9].

$$\eta = \frac{W_{rec}}{W_{rec}+W_{loss}} \quad (2)$$

where W_{loss} is the hysteresis loss. The breakdown electric field (E_{BD}) is also an essential factor for energy storage; i.e., a higher DBS is responsible for a large energy storage density. Thus, lead-based RFE and AFE materials have been widely investigated for energy storage applications [10,11]. However, lead is hazardous to the environment and human health and non-eco-friendly due to its toxicity, which has motivated the development of alternative lead-free materials. In recent years, lead-free RFEs and AFEs, such as $BaTiO_3$ (BT) [12,13], $Bi_{0.5}Na_{0.5}TiO_3$ (BNT) [6,14,15], $BiFeO_3$ (BFO) [16,17], and $NaNbO_3$ (NN) [18]-based materials with boosted energy storage performance have been reported for applications in energy storage devices.

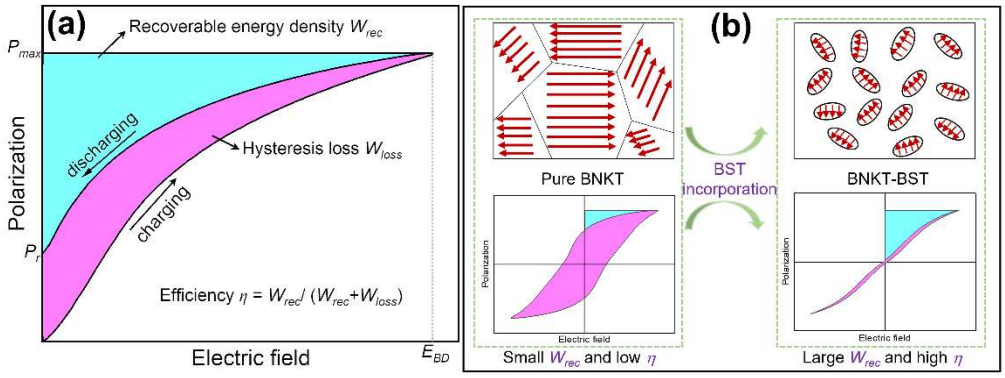

Figure 1. Schematic diagram of (a) recoverable energy density and hysteresis loss from P–E hysteresis loop of a dielectric material. (b) Domain evolution and formation of FE to RFE transition with the substitution of BST into BNKT, resulting in enhanced W_{rec} and η.

The perovskite-structured BNT-based ceramics exhibit a strong ferroelectric response, since Bi^{3+} has a lone pair of electrons ($6s^2$), which strongly hybridizes with the oxygen 2p orbital [19]. Furthermore, the formation of highly-dynamic polar nano-regions (PNRs) are facilitated by the local random fields induced by valency differences and compositional inhomogeneity [20,21]. Moreover, the relaxor behavior of the material can be improved by adding another phase with a similar perovskite to form a solid solution or modifying the base compound with a suitable dopant, which enables slim P-E loops [22]. Sayyed et al. [23] investigated the local structural deformation and dielectric anomalies near the morphotropic phase boundary (MPB) of (1-x) $Na_{0.5}Bi_{0.5}TiO_3$-x$SrTiO_3$ ceramics. The ferroelectric response of (1-x) $Na_{0.5}Bi_{0.5}TiO_3$-$SrTiO_3$-x$AgNbO_3$ ceramics is similar to the antiferroelectric response and provided improved energy storage performance [24]. Shi et al. [25] reported that Zr and Sm doped 0.74$Na_{0.5}Bi_{0.5}TiO_3$-0.26$SrTiO_3$ ceramics significantly enhanced energy storage performance and the DBS. $Bi_{0.2}Sr_{0.7}TiO_3$ (BST) exhibits a strong polarization and wide phase transition temperature with diffused dielectric maxima. It was incorporated into BNT ceramics, suppressing the field-generated ferroelectric phase and achieving a large P_{max} and small P_r [26,27]. Recently, Li et al. reported a synergistic approach to enhance the energy storage response in BNT-based RFEs by introducing PNRs and lowered the transition temperature by stabilizing the AFE responses at low temperatures [9].

In this work, we investigate a domain engineering process to improve energy storage performance by modifying $Bi_{0.5}(Na_{0.8}K_{0.2})_{0.5}TiO_3$ (BNKT) RFEs with BST. It is demonstrated that the addition of BST can transform the ferroelectric microdomains of BNKT into highly-dynamic PNRs. This results in a macroscopic ferroelectric to relaxor ferroelectric transition as schematically

 doi:10.20944/preprints202306.0591.v1

illustrated in Figure 1b. The favorable relaxor ferroelectric state formed by the domain engineering method simultaneously produces a large P_{max} and reduced P_r, which facilitates the enhancement of DBS with the BST, resulting in high energy density and high efficiency of the BNKT-BST RFES.

2. Materials and Methods

First, (1-x)$Bi_{0.5}(Na_{0.8}K_{0.2})_{0.5}TiO_3$-x$Bi_{0.2}Sr_{0.7}TiO_3$ (BNKT-BST; x = 0.15, 0.30, 0.40, 0.45 and 0.50) RFE ceramics were fabricated by a solid-state reaction method. To prepare BNKT and BST, high-purity raw materials of Bi_2O_3, (Sigma-Aldrich, 99.9%), Na_2CO_3 (Sigma-Aldrich, 99.5%), K_2CO_3 (Sigma-Aldrich, 99%), TiO_2, (Sigma-Aldrich, 99%), and $SrCO_3$ (Sigma-Aldrich, 98%) were weighed according to the nominal stoichiometric compositions and then ball-milled using a planetary ball mill for 24h with ZrO_2 balls in ethanol. After the slurries were dried at 120 °C, the mixture of BNKT and BST powders was calcined at 800 °C and 950 °C for 2h and 3h, respectively, to form a pure phase of $Bi_{0.5}(Na_{0.8}K_{0.2})_{0.5}TiO_3$ and $Bi_{0.2}Sr_{0.7}TiO_3$. Both BNKT and BST calcined powders were mixed and ball milled for 12h to prepare a BNKT-BST composition. Further, these powders were granulated with 5 wt.% polyvinyl alcohol and uniaxially pressed into disks at a pressure of 10 MPa in a 10 mm diameter and ~0.5 mm thickness followed by sintered at 1100 °C for 3h. To perform electrical measurements, a silver paste was coated on both sides of the sintered disks.

The phase formation of the BNKT-BST ceramic samples was examined using an X-ray diffractometer (Rigaku, TTRAX III 18 kW) with monochromatic Cu-Kα radiation (λ =1.5406 Å). Raman spectra was recorded using a Raman spectrometer (JOBIN YVON, LABRAM HR800) with a laser wavelength of 532.06 nm. Surface morphology was investigated by a field emission scanning electron microscope (FESEM) (JEOL, JSM-7610F). Temperature and frequency-dependent dielectric properties were measured from room temperature (RT) to 400 °C and 1 kHz – 1 MHz using an impedance analyzer (Hewlett Packard, 4294A). P-E and I-E loops were measured using a ferroelectric tester (Aix ACT, TF Analyzer 2000).

3. Results and discussion

3.1. Phase evolution and microstructure

Figure 2a shows the X-ray diffraction (XRD) patterns of BNKT-BST ceramics (x = 0.15 – 0.50) in the 2θ range of 20–70°. All the samples revealed a rhombohedral and tetragonal crystal structure, which indicates the diffusion of BST into BNKT and the formation of a BNKT-BST as a homogeneous solid solution. At RT, the BNKT system exhibits a rhombohedral and tetragonal crystal structure near MPB at x = 0.16–0.2 [28,29]. The formation of MPB in BNKT-BST ceramics is confirmed by the splitting of the (021)/(111) and (122)/(211) peaks at 2θ around 40° and 58°, respectively, are shown in Figure 2b. In addition, both the (021) and (122) peaks shifted slightly towards lower angles with increasing BST into BNKT, demonstrating enhanced lattice parameters. The enhancement of lattice parameters can be attributed to the ionic radius of Sr^{2+} (1.44 Å), which is larger than that of Bi^{3+} (1.36 Å), Na^+ (1.39 Å), and K^+ (1.38 Å), respectively, at the A-site [30–32]. Figure 2c shows the Raman spectra of BNKT-BST along with spectral de-convolution in the Raman shift of 50–1000 cm^{-1}. The Raman spectra of all compositions are similar to the previous reports of BNKT-based ceramics [33]. The Raman active bands are divided into four Raman vibration modes, as shown at the top of Figure 2c. (i) the modes below 200 cm^{-1} related to the vibration of A-site (Bi-O, Na-O, K-O, and Sr-O), (ii) the modes between 200–440 cm^{-1} correspond to the vibrations of B–O (Ti-O), (iii) the modes between 440–700 cm^{-1} correspond to the vibrations of BO_6 (TiO_6)-octahedra, and (iv) the modes above 700 cm^{-1} are related to the A1 and E (longitudinal optical) overlapping modes [33]. The modes appearing at 124–172 cm^{-1}, and 768 cm^{-1} are shifted to higher wavenumber of 128–189 cm^{-1} and 779 cm^{-1} with BST, associated with the A-site, and A1+E vibrations caused by A-site disorder. Such disorder is induced by the incorporation of BST (Bi^{3+}, and Sr^{2+}) into the BNKT (Bi^{3+}, Na^+ and K^+) system [34]. In addition, a noticeable change at 250 and 320 cm^{-1} shifted towards lower wavenumber of 233, and 305 cm^{-1} with BST, which is caused by an increase in the B-site disorder in the BNKT-BST system [31]. Moreover, these modes are slightly broadened, confirming the disturbance of the long-range ferroelectric order

Preprints (www.preprints.org) | NOT PEER-REVIEWED | Posted: 8 June 2023 doi:10.20944/preprints202306.0591.v1

and the formation of highly dynamic PNRs, and this improves the relaxor characteristics of BNKT-BST. This result is consistent with the XRD and electrical properties presented in sections 3.2 and 3.3.

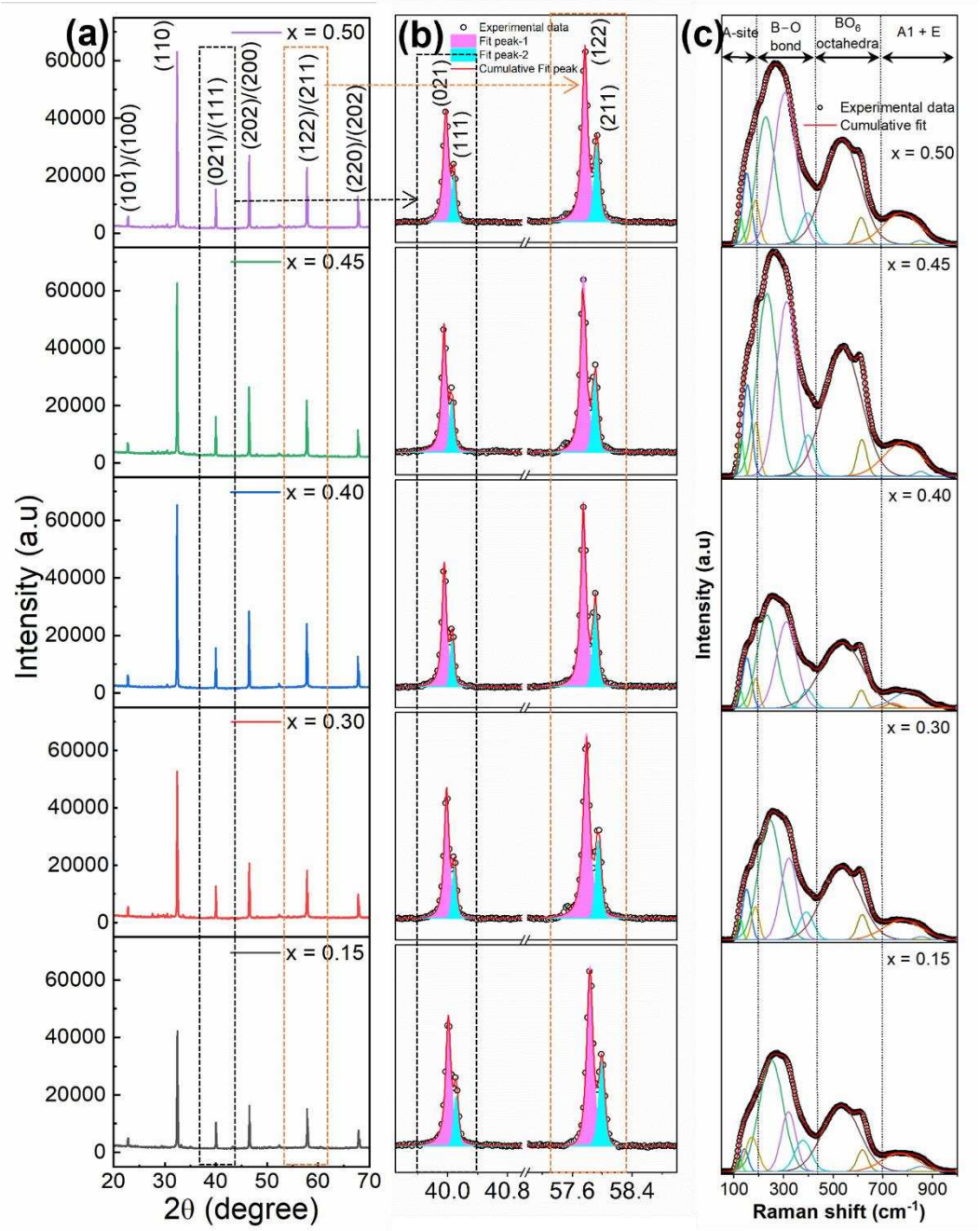

Figure 2. (a) XRD patterns of the (1-x)BNKT-xBST ceramics for x=0.15–050, where (b) 2θ = 39 – 59°. (c) Raman spectra of BNKT-BST ceramics along with spectral deconvolution.

Figure 3 shows FESEM images of the BNKT-BST ceramics. All the ceramics display rectangular-shaped grains, which are homogeneously distributed. Figure 3(d) clearly shows that the x=0.45 composition exhibits a highly dense microstructure and is more compact with smaller grains as compared to the other samples of BNKT-BST (x<0.45 and x=0.50). The average grain size of the BNKT-BST samples was calculated by the linear intercept method using Image-J software and found to be 1.37 μm for the x=0.15 composition and is gradually enhanced to 1.6 μm with the incorporation of BST. The grain size enhancement is caused by the generation of oxygen vacancies by Sr^{2+} entering the perovskite of BNKT and substituting at the A-site of Bi^{3+}, Na^{+}, and K^{+} [35]. Previous reports

Preprints (www.preprints.org) | NOT PEER-REVIEWED | Posted: 8 June 2023 doi:10.20944/preprints202306.0591.v1

investigated that the fine grain size with homogeneous and dense microstructure can withstand higher electric fields, leads to high DBS, and improve energy storage performance [36,37].

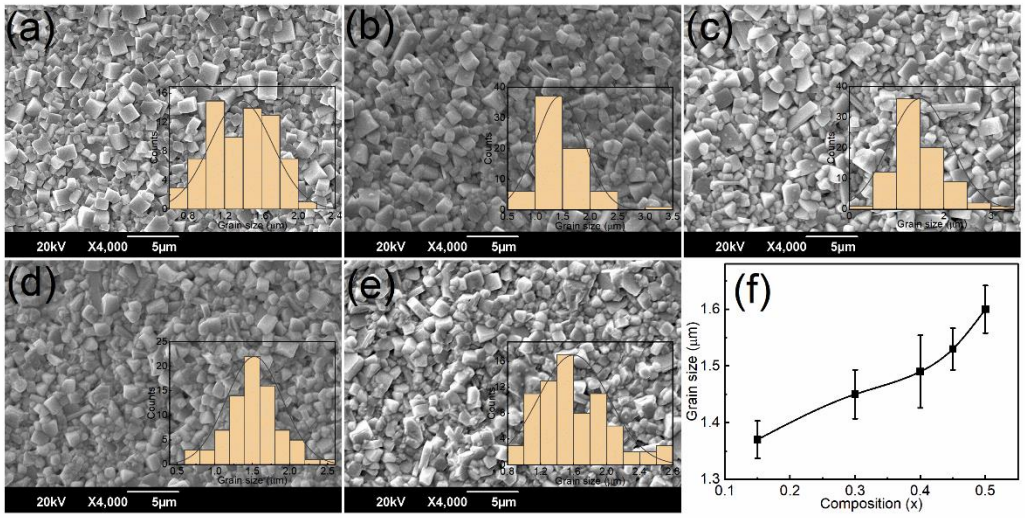

Figure 3. FESEM images with grain size distribution (inset) of (1-x)BNKT-xBST ceramics for (a) x =0.15, (b) x=0.30, (c) x=0.40, (d) x=0.45 and (e) x=0.50. (f) Composition (x) versus grain size.

3.2. Dielectric properties and relaxor behaviour

Figure 4a displays the frequency variation of relative dielectric permittivity (ε_r) and loss factor ($tan\delta$) of BNKT-BST ceramic capacitors, measured at RT in the range of 1 kHz to 1 MHz. The sample x=0.15 displayed a higher ε_r of 1481 and $tan\delta$ of 0.231 at 1 kHz than pure BNKT (ε_r of 1273 and $tan\delta$ of 0.047 at 1 kHz) reported in our previous report [29]. These ε_r values are gradually enhanced to 2664 and the $tan\delta$ values are reduced to 0.058 for the x = 0.45 sample (Figure 4b). The enhancement of the dielectric properties is attributed to the incorporation of BST into BNKT and the dense microstructure.

Figure 4c displays the temperature variation of ε_r and $tan\delta$ of BNKT-BST for the x = 0.45 composition, measured from RT to 400 °C at various frequencies (0.1 kHz to 1 MHz). It was observed that the dielectric maximum temperature (T_m) shifted towards a lower temperature ~53 °C as compared to pure BNKT (300 °C) [29]. The incorporation of BST into BNKT can disturb the long-range ferroelectric order, resulting in a lowered T_m. This lower T_m leads to the formation of highly-dynamic PNRs due to the mismatch of the ionic radius at the A-site of BNKT-BST. In addition, the T_m shifted towards higher temperatures, and dielectric peaks diffused with an increase in frequency. This frequency dispersion with a diffuse phase transition reveals typical relaxor ferroelectric characteristics [38,39]. The degree of the relaxor characteristics was determined using the modified Curie-Weiss law by the following equation [40,41].

$$\left(1/\varepsilon_r\right) - \left(1/\varepsilon_r^m\right) = (T - T_m)^\gamma / C \qquad (3)$$

where, ε_r^m is the maximum relative dielectric permittivity at the maximum temperature T_m, T is the temperature, γ is the degree of relaxation, and C is the Curie constant. Generally, the γ value is 1 for normal ferroelectrics and between 1 and 2 for relaxor ferroelectrics [40]. The obtained γ value is 1.83 indicating typical relaxor ferroelectric characteristics, which is consistent with Raman results.

Preprints (www.preprints.org) | NOT PEER-REVIEWED | Posted: 8 June 2023 doi:10.20944/preprints202306.0591.v1

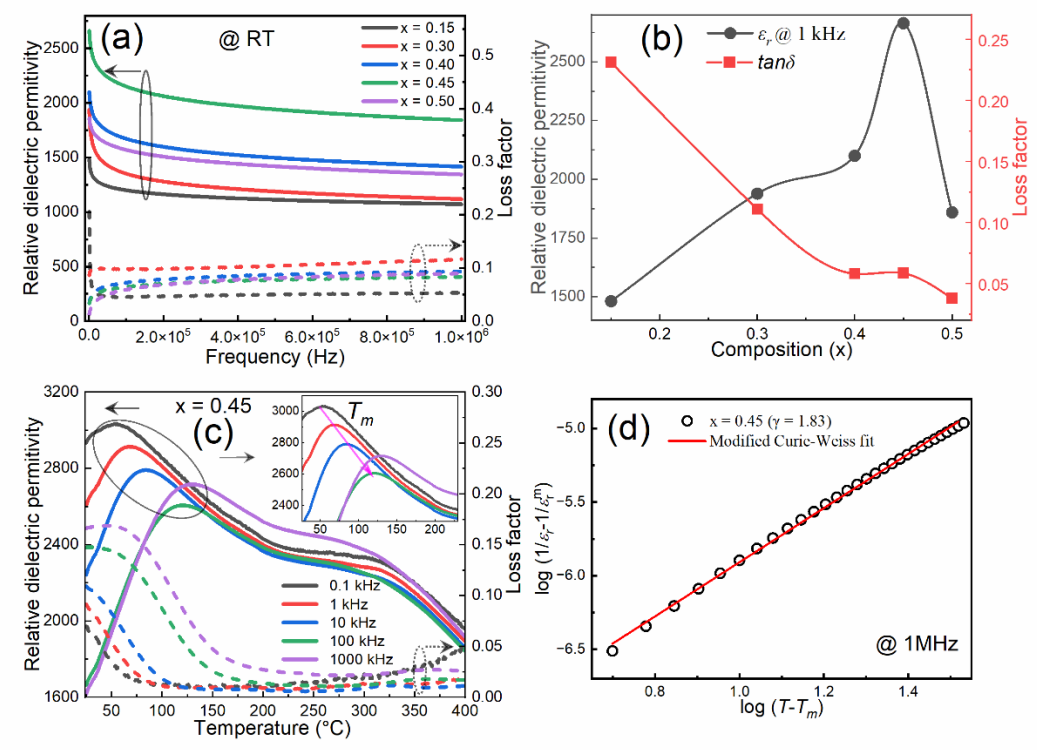

Figure 4. (a) Frequency variation of relative dielectric permittivity and loss factor of BNKT-BST ceramics (x=0.15-0.50). (b) Composition versus relative dielectric permittivity and loss factor. (d) Temperature variation of relative dielectric permittivity and loss factor of BNKT-BST for x=0.45. The inset of Figure 4(c) shows the shift in T_m towards high temperatures with frequency. (d) $log(T - T_m)$ versus $log\left[\left(1/\varepsilon_r\right) - \left(1/\varepsilon_r^m\right)\right]$ of BNKT-BST (x = 0.45) at 1 MHz.

3.3. FE-RFE transformation, domain evolution, and energy storage performance

Figure 5 displays the RT bipolar P-E hysteresis loops and current (I)-electric field (E) curves of BNKT-BST ceramic capacitors measured at various electric fields and 10 Hz. The BNKT-BST (x=0.15) sample exhibits a typical ferroelectric (FE) characteristic, displaying high remnant polarization P_r of 19.89 μC/cm², high maximum polarization P_{max} of 31.46 μC/cm², and a high coercive field E_c of 16.66 kV/cm. These values gradually decreased, whereas the E_{max} or E_{BD} increased from 57.42 kV/cm to 90 kV/cm with the incorporation of BST (x=0.45), which is favorable for high energy storage density (Figure 5f). It was evident that the two peaks in the I-E curves (x≥0.30) and slim P-E loops are attributed to the formation of highly dynamic PNRs, which can be commonly seen in RFEs [42]. In general, the P-E loops present in normal FEs are due to the macroscopic domain wall motion, while in RFEs, highly-dynamic PNRs exist instead of macrodomains, resulting in slim P-E loops [43].

Preprints (www.preprints.org) | NOT PEER-REVIEWED | Posted: 8 June 2023 doi:10.20944/preprints202306.0591.v1

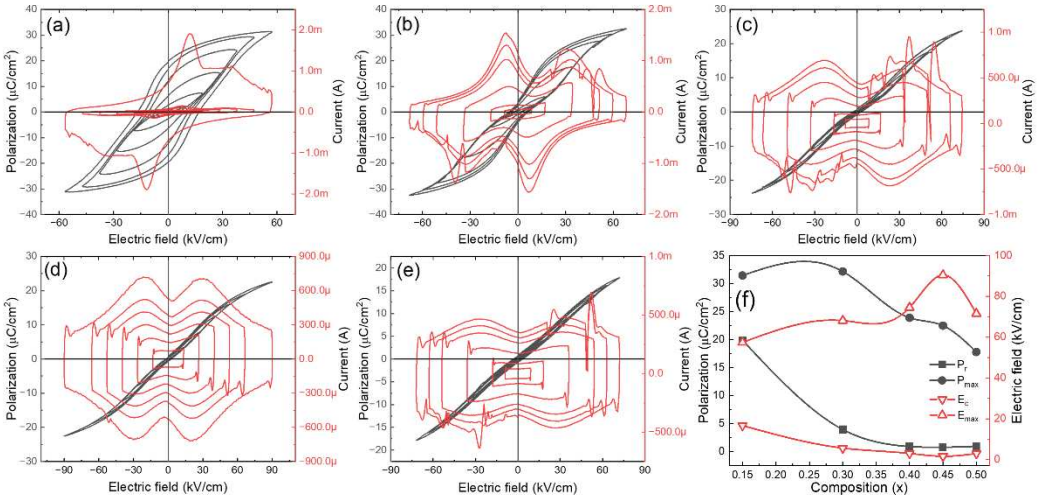

Figure 5. RT P-E and I-E curves of BNKT-BST ceramics for (a) x =0.15, (b) x=0.30, (c) x=0.40, (d) x=0.45, and (e) x=0.50. (f) Composition (x) versus polarization and electric field.

Further, the W_{rec} was calculated by equation (1) from P-E loops, which are shown in Figure 6 (cyan shaded area). The W_{loss} is calculated by the enclosed area of the P-E loops in the first quadrant (magenta shaded area), and η is calculated by equation (2) [44]. The W_{rec} values gradually increased and the W_{loss} values decreased with the substitution of BST, and the composition x=0.45 displays a high energy density of 0.81 J/cm^3 at E_{BD} of 90 kV/cm and high energy efficiency of 86.95% (Figure 6f). The improvement in the energy storage performance is achieved by the domain engineering method by modifying BNKT with BST. It can be understood that the substitution of BST can transform the ferroelectric microdomains of BNKT into highly-dynamic PNRs, resulting in a macroscopic FE to RFE transition. This domain evolution and transformation of FE to RFE transition in present samples as schematically shown in Figure 1b. The highly-dynamic PNRs induced large P_{max} and low P_r, which together improved the DBS with the incorporation of BST, resulting in high energy storage density and high energy efficiency of the BNKT-BST RFEs [44]. The obtained W_{rec} and η of 0.55 BNKT- 0.45 BST are comparable/superior to other lead-free RFEs and are promising for energy storage capacitors [42,44–47].

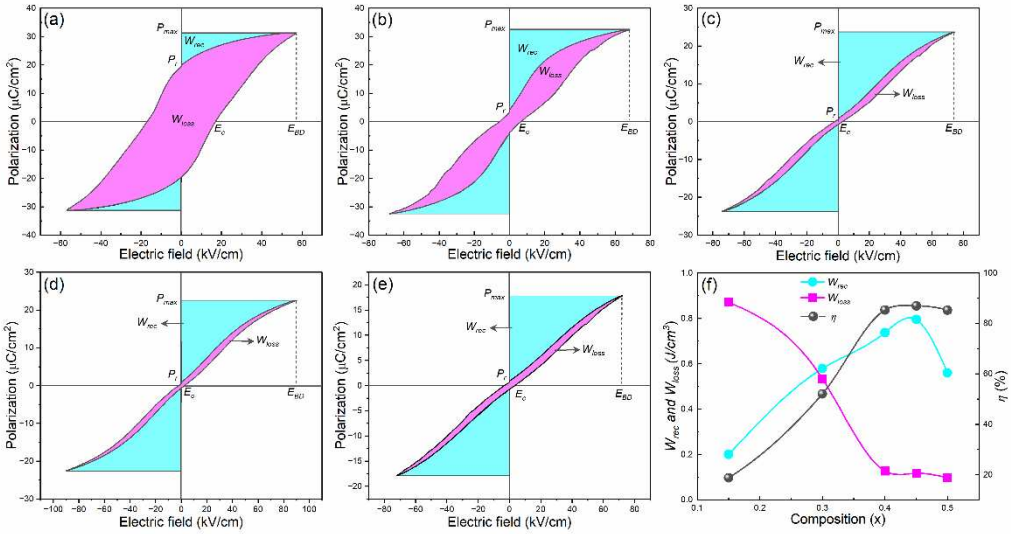

Figure 6. P-E loops of BNKT-BST ceramics measured at E_{BD} and 10 Hz for (a) x =0.15, (b) x=0.30, (c) x=0.40, (d) x=0.45 and (e) x=0.50. (f) Composition (x) versus W_{rec}, W_{loss} and η.

4. Conclusions

The domain-engineered relaxor ferroelectric BNKT-BST ceramics were fabricated by a solid-state reaction method and demonstrated structural, microstructural, dielectric, and ferroelectric properties in detail. XRD, Raman spectra, and FESEM studies revealed the formation of a rhombohedral–tetragonal phase, highly dynamic PNRs, and dense microstructure. The dielectric properties are improved with BST, and a high ε_r of 2664 and low $tan\delta$ of 0.058 at 1 kHz were obtained for x=0.45 composition. The incorporation of BST into BNKT can disturb the long-range ferroelectric order, causing lowered T_m and the formation of highly-dynamic PNRs. In addition, the T_m shifts toward high temperature with frequency and diffuse phase transition, indicating relaxor ferroelectric characteristics of BNKT-BST ceramics, and is confirmed by the modified Curie Weiss law. The rhombohedral–tetragonal phase, fine grain size, and lowered T_m with relaxor properties simultaneously contribute to a high P_{max} and low P_r. This improved the DBS and gives rise to giant energy-storage density and high energy efficiency of the BNKT-BST RFEs, which makes this material is a good candidate for pulse driving energy storage applications.

Author Contributions: Conceptualization, measurement, data curation, investigation, visualization, writing—original draft preparation, review and editing, S. P.; data curation, formal analysis, H. C.; data curation, Y.L.; writing – review & editing, K. P.; writing – review & editing, K. C.; validation, project administration, writing – review & editing, supervision, G. H. All authors have read and agreed to the published version of the manuscript.

Funding: This research was funded by an NRF grant funded by the Korean government (MSIT) (No. 2022R1A2C4001497).

Institutional Review Board Statement: Not applicable.

Informed Consent Statement: Not applicable.

Data Availability Statement: Not applicable.

Conflicts of Interest: The authors declare no conflict of interest.

References

1. Shen, Y.; Zhang, X.; Li, M.; Lin, Y.; Nan, C.-W. Polymer Nanocomposite Dielectrics for Electrical Energy Storage. *Natl Sci Rev* **2017**, *4*, 23–25, doi:10.1093/nsr/nww066.
2. Yao, Z.; Song, Z.; Hao, H.; Yu, Z.; Cao, M.; Zhang, S.; Lanagan, M.T.; Liu, H. Homogeneous/Inhomogeneous-Structured Dielectrics and Their Energy-Storage Performances. *Advanced Materials* **2017**, *29*, 1601727, doi:10.1002/adma.201601727.
3. Palneedi, H.; Peddigari, M.; Hwang, G.-T.; Jeong, D.-Y.; Ryu, J. High-Performance Dielectric Ceramic Films for Energy Storage Capacitors: Progress and Outlook. *Adv Funct Mater* **2018**, *28*, 1803665, doi:10.1002/adfm.201803665.
4. Li, Q.; Chen, L.; Gadinski, M.R.; Zhang, S.; Zhang, G.; Li, H.U.; Iagodkine, E.; Haque, A.; Chen, L.-Q.; Jackson, T.N.; et al. Flexible High-Temperature Dielectric Materials from Polymer Nanocomposites. *Nature* **2015**, *523*, 576–579, doi:10.1038/nature14647.
5. Kumar, N.; Ionin, A.; Ansell, T.; Kwon, S.; Hackenberger, W.; Cann, D. Multilayer Ceramic Capacitors Based on Relaxor $BaTiO_3$-$Bi(Zn_{1/2}Ti_{1/2})O_3$ for Temperature Stable and High Energy Density Capacitor Applications. *Appl Phys Lett* **2015**, *106*, 252901, doi:10.1063/1.4922947.
6. Li, J.; Li, F.; Xu, Z.; Zhang, S. Multilayer Lead-Free Ceramic Capacitors with Ultrahigh Energy Density and Efficiency. *Advanced Materials* **2018**, *30*, 1802155, doi:10.1002/adma.201802155.
7. Chen, Q.; Shen, Y.; Zhang, S.; Zhang, Q.M. Polymer-Based Dielectrics with High Energy Storage Density. *Annu Rev Mater Res* **2015**, *45*, 433–458, doi:10.1146/annurev-matsci-070214-021017.
8. Xie, A.; Zuo, R.; Qiao, Z.; Fu, Z.; Hu, T.; Fei, L. $NaNbO_3$ -$(Bi_{0.5}Li_{0.5})TiO_3$ Lead-Free Relaxor Ferroelectric Capacitors with Superior Energy-Storage Performances via Multiple Synergistic Design. *Adv Energy Mater* **2021**, *11*, 2101378, doi:10.1002/aenm.202101378.
9. Li, T.; Jiang, X.; Li, J.; Xie, A.; Fu, J.; Zuo, R. Ultrahigh Energy-Storage Performances in Lead-Free $Na_{0.5}Bi_{0.5}TiO_3$ -Based Relaxor Antiferroelectric Ceramics through a Synergistic Design Strategy. *ACS Appl Mater Interfaces* **2022**, *14*, 22263–22269, doi:10.1021/acsami.2c01287.
10. Zhang, G.; Zhu, D.; Zhang, X.; Zhang, L.; Yi, J.; Xie, B.; Zeng, Y.; Li, Q.; Wang, Q.; Jiang, S. High-Energy Storage Performance of $(Pb_{0.87}Ba_{0.1}La_{0.02})(Zr_{0.68}Sn_{0.24}Ti_{0.08})O_3$ Antiferroelectric Ceramics Fabricated by

the Hot-Press Sintering Method. *Journal of the American Ceramic Society* **2015**, *98*, 1175–1181, doi:10.1111/jace.13412.

11. Liu, Z.; Chen, X.; Peng, W.; Xu, C.; Dong, X.; Cao, F.; Wang, G. Temperature-Dependent Stability of Energy Storage Properties of Pb $_{0.97}$ La $_{0.02}$ (Zr $_{0.58}$ Sn $_{0.335}$ Ti $_{0.085}$)O $_3$ Antiferroelectric Ceramics for Pulse Power Capacitors. *Appl Phys Lett* **2015**, *106*, 262901, doi:10.1063/1.4923373.
12. Yuan, Q.; Li, G.; Yao, F.-Z.; Cheng, S.-D.; Wang, Y.; Ma, R.; Mi, S.-B.; Gu, M.; Wang, K.; Li, J.-F.; et al. Simultaneously Achieved Temperature-Insensitive High Energy Density and Efficiency in Domain Engineered $BaTiO_3$-$Bi(Mg_{0.5}Zr_{0.5})O_3$ Lead-Free Relaxor Ferroelectrics. *Nano Energy* **2018**, *52*, 203–210, doi:10.1016/j.nanoen.2018.07.055.
13. Zhao, P.; Wang, H.; Wu, L.; Chen, L.; Cai, Z.; Li, L.; Wang, X. High-Performance Relaxor Ferroelectric Materials for Energy Storage Applications. *Adv Energy Mater* **2019**, *9*, 1803048, doi:10.1002/aenm.201803048.
14. Yin, J.; Zhang, Y.; Lv, X.; Wu, J. Ultrahigh Energy-Storage Potential under Low Electric Field in Bismuth Sodium Titanate-Based Perovskite Ferroelectrics. *J Mater Chem A Mater* **2018**, *6*, 9823–9832, doi:10.1039/C8TA00474A.
15. Qi, H.; Zuo, R. Linear-like Lead-Free Relaxor Antiferroelectric (Bi $_{0.5}$ Na $_{0.5}$)TiO $_3$ –NaNbO $_3$ with Giant Energy-Storage Density/Efficiency and Super Stability against Temperature and Frequency. *J Mater Chem A Mater* **2019**, *7*, 3971–3978, doi:10.1039/C8TA12232F.
16. Wang, G.; Li, J.; Zhang, X.; Fan, Z.; Yang, F.; Feteira, A.; Zhou, D.; Sinclair, D.C.; Ma, T.; Tan, X.; et al. Ultrahigh Energy Storage Density Lead-Free Multilayers by Controlled Electrical Homogeneity. *Energy Environ Sci* **2019**, *12*, 582–588, doi:10.1039/C8EE03287D.
17. Pan, H.; Li, F.; Liu, Y.; Zhang, Q.; Wang, M.; Lan, S.; Zheng, Y.; Ma, J.; Gu, L.; Shen, Y.; et al. Ultrahigh–Energy Density Lead-Free Dielectric Films via Polymorphic Nanodomain Design. *Science (1979)* **2019**, *365*, 578–582, doi:10.1126/science.aaw8109.
18. Qi, H.; Zuo, R.; Xie, A.; Tian, A.; Fu, J.; Zhang, Y.; Zhang, S. Ultrahigh Energy-Storage Density in $NaNbO_3$-Based Lead-Free Relaxor Antiferroelectric Ceramics with Nanoscale Domains. *Adv Funct Mater* **2019**, *29*, 1903877, doi:10.1002/adfm.201903877.
19. Li, F.; Hou, X.; Wang, J.; Zeng, H.; Shen, B.; Zhai, J. Structure-Design Strategy of 0–3 Type $(Bi_{0.32}Sr_{0.42}Na_{0.20})TiO_3$/MgO Composite to Boost Energy Storage Density, Efficiency and Charge-Discharge Performance. *J Eur Ceram Soc* **2019**, *39*, 2889–2898, doi:10.1016/j.jeurceramsoc.2019.03.047.
20. Liu, N.; Liang, R.; Zhou, Z.; Dong, X. Designing Lead-Free Bismuth Ferrite-Based Ceramics Learning from Relaxor Ferroelectric Behavior for Simultaneous High Energy Density and Efficiency under Low Electric Field. *J Mater Chem C Mater* **2018**, *6*, 10211–10217, doi:10.1039/C8TC03855D.
21. Wu, Y.; Fan, Y.; Liu, N.; Peng, P.; Zhou, M.; Yan, S.; Cao, F.; Dong, X.; Wang, G. Enhanced Energy Storage Properties in Sodium Bismuth Titanate-Based Ceramics for Dielectric Capacitor Applications. *J Mater Chem C Mater* **2019**, *7*, 6222–6230, doi:10.1039/C9TC01239G.
22. Hu, Q.; Tian, Y.; Zhu, Q.; Bian, J.; Jin, L.; Du, H.; Alikin, D.O.; Shur, V.Y.; Feng, Y.; Xu, Z.; et al. Achieve Ultrahigh Energy Storage Performance in $BaTiO_3$–$Bi(Mg_{1/2}Ti_{1/2})O_3$ Relaxor Ferroelectric Ceramics via Nano-Scale Polarization Mismatch and Reconstruction. *Nano Energy* **2020**, *67*, 104264, doi:10.1016/j.nanoen.2019.104264.
23. Sayyed, S.; Acharya, S.A.; Kautkar, P.; Sathe, V. Structural and Dielectric Anomalies near the MPB Region of Na $_{0.5}$ Bi $_{0.5}$ TiO $_3$ –SrTiO $_3$ Solid Solution. *RSC Adv* **2015**, *5*, 50644–50654, doi:10.1039/C5RA05617A.
24. Ma, W.; Zhu, Y.; Marwat, M.A.; Fan, P.; Xie, B.; Salamon, D.; Ye, Z.-G.; Zhang, H. Enhanced Energy-Storage Performance with Excellent Stability under Low Electric Fields in BNT–ST Relaxor Ferroelectric Ceramics. *J Mater Chem C Mater* **2019**, *7*, 281–288, doi:10.1039/C8TC04447C.
25. Shi, L.N.; Wang, Y.G.; Ren, Z.H.; Jain, A.; Jiang, S.S.; Chen, F.G. Significant Improvement in Electrical Characteristics and Energy Storage Performance of NBT-Based Ceramics. *Ceram Int* **2022**, *48*, 26973–26983, doi:10.1016/j.ceramint.2022.06.009.
26. Kong, X.; Yang, L.; Cheng, Z.; Zhang, S. Bi-modified $SrTiO_3$ -based Ceramics for High-temperature Energy Storage Applications. *Journal of the American Ceramic Society* **2020**, *103*, 1722–1731, doi:10.1111/jace.16844.
27. Wei, T.; Liu, K.; Fan, P.; Lu, D.; Ye, B.; Zhou, C.; Yang, H.; Tan, H.; Salamon, D.; Nan, B.; et al. Novel $NaNbO_3$–$Sr_{0.7}Bi_{0.2}TiO_3$ Lead-Free Dielectric Ceramics with Excellent Energy Storage Properties. *Ceram Int* **2021**, *47*, 3713–3719, doi:10.1016/j.ceramint.2020.09.228.
28. Pham, K.-N.; Hussain, A.; Ahn, C.W.; Kim, W.; Jeong, S.J.; Lee, J.-S. Giant Strain in Nb-Doped $Bi_{0.5}(Na_{0.82}K_{0.18})_{0.5}TiO_3$ Lead-Free Electromechanical Ceramics. *Mater Lett* **2010**, *64*, 2219–2222, doi:10.1016/j.matlet.2010.07.048.
29. Pattipaka, S.; James, A.R.; Dobbidi, P. Dielectric, Piezoelectric and Variable Range Hopping Conductivity Studies of $Bi_{0.5}(Na, K)_{0.5}TiO_3$ Ceramics. *J Electron Mater* **2018**, *47*, 3876–3890, doi:10.1007/s11664-018-6263-0.

30. Gupta, S.K.; McQuade, R.; Gibbons, B.; Mardilovich, P.; Cann, D.P. Electric Field-Induced Strain in Sr(Hf 0.5 Zr 0.5)O 3 -Modified Bi 0.5 (Na 0.8 K 0.2) 0.5 TiO 3 Piezoelectric Ceramics. *J Appl Phys* **2020**, *127*, 074104, doi:10.1063/1.5132536.
31. Pattipaka, S.; James, A.R.; Dobbidi, P. Enhanced Dielectric and Piezoelectric Properties of BNT-KNNG Piezoelectric Ceramics. *J Alloys Compd* **2018**, *765*, 1195–1208, doi:10.1016/j.jallcom.2018.06.138.
32. Tong, X.-Y.; Song, M.-W.; Zhou, J.-J.; Wang, K.; Guan, C.-L.; Liu, H.; Fang, J.-Z. Enhanced Energy Storage Properties in Nb-Modified $Bi_{0.5}Na_{0.5}TiO_3$–$SrTiO_3$ Lead-Free Electroceramics. *Journal of Materials Science: Materials in Electronics* **2019**, *30*, 5780–5790, doi:10.1007/s10854-019-00876-2.
33. Jaita, P.; Saenkam, K.; Rujijanagul, G. Improvements in Piezoelectric and Energy Harvesting Properties with a Slight Change in Depolarization Temperature in Modified BNKT Ceramics by a Simple Technique. *RSC Adv* **2023**, *13*, 3743–3758, doi:10.1039/D2RA07587C.
34. Chu, B.; Hao, J.; Li, P.; Li, Y.; Li, W.; Zheng, L.; Zeng, H. High-Energy Storage Properties over a Broad Temperature Range in La-Modified BNT-Based Lead-Free Ceramics. *ACS Appl Mater Interfaces* **2022**, *14*, 19683–19696, doi:10.1021/acsami.2c01863.
35. Zhang, H.; Zhou, J.; Shen, J.; Yang, X.; Wu, C.; Han, K.; Zhao, Z.; Chen, W. Enhanced Piezoelectric Property and Promoted Depolarization Temperature in Fe Doped $Bi_{1/2}(Na_{0.8}K_{0.2})_{1/2}TiO_3$ Lead-Free Ceramics. *Ceram Int* **2017**, *43*, 16395–16402, doi:10.1016/j.ceramint.2017.09.015.
36. Huang, Y.; Zhao, C.; Wu, B.; Wu, J. Multifunctional $BaTiO_3$-Based Relaxor Ferroelectrics toward Excellent Energy Storage Performance and Electrostrictive Strain Benefiting from Crossover Region. *ACS Appl Mater Interfaces* **2020**, *12*, 23885–23895, doi:10.1021/acsami.0c03677.
37. Sun, Z.; Wang, Z.; Tian, Y.; Wang, G.; Wang, W.; Yang, M.; Wang, X.; Zhang, F.; Pu, Y. Progress, Outlook, and Challenges in Lead-Free Energy-Storage Ferroelectrics. *Adv Electron Mater* **2020**, *6*, 1900698, doi:10.1002/aelm.201900698.
38. Shvartsman, V. V.; Lupascu, D.C. Lead-Free Relaxor Ferroelectrics. *Journal of the American Ceramic Society* **2012**, *95*, 1–26, doi:10.1111/j.1551-2916.2011.04952.x.
39. Liu, G.; Wang, Y.; Han, G.; Gao, J.; Yu, L.; Tang, M.; Li, Y.; Hu, J.; Jin, L.; Yan, Y. Enhanced Electrical Properties and Energy Storage Performances of NBT-ST Pb-Free Ceramics through Glass Modification. *J Alloys Compd* **2020**, *836*, 154961, doi:10.1016/j.jallcom.2020.154961.
40. Uchino, K.; Nomura, S.; Cross, L.E.; Jang, S.J.; Newnham, R.E. Electrostrictive Effect in Lead Magnesium Niobate Single Crystals. *J Appl Phys* **1980**, *51*, 1142–1145, doi:10.1063/1.327724.
41. Gupta, S.K.; McQuade, R.; Gibbons, B.; Mardilovich, P.; Cann, D.P. Electric Field-Induced Strain in Sr(Hf 0.5 Zr 0.5)O 3 -Modified Bi 0.5 (Na 0.8 K 0.2) 0.5 TiO 3 Piezoelectric Ceramics. *J Appl Phys* **2020**, *127*, 074104, doi:10.1063/1.5132536.
42. Li, Q.; Wang, C.; Yadav, A.K.; Fan, H. Large Electrostrictive Effect and Energy Storage Density in $MnCO_3$ Modified $Na_{0.325}Bi_{0.395}Sr_{0.245}\square_{0.035}TiO_3$ Lead-Free Ceramics. *Ceram Int* **2020**, *46*, 3374–3381, doi:10.1016/j.ceramint.2019.10.047.
43. Yang, L.; Kong, X.; Li, F.; Hao, H.; Cheng, Z.; Liu, H.; Li, J.-F.; Zhang, S. Perovskite Lead-Free Dielectrics for Energy Storage Applications. *Prog Mater Sci* **2019**, *102*, 72–108, doi:10.1016/j.pmatsci.2018.12.005.
44. Wu, J.; Mahajan, A.; Riekehr, L.; Zhang, H.; Yang, B.; Meng, N.; Zhang, Z.; Yan, H. Perovskite $Sr_x(Bi_{1-x}Na_{0.97-x}Li_{0.03})_{0.5}TiO_3$ Ceramics with Polar Nano Regions for High Power Energy Storage. *Nano Energy* **2018**, *50*, 723–732, doi:10.1016/j.nanoen.2018.06.016.
45. Yan, Y.; Zeng, X.; Deng, T.; Chen, F.; Yang, L.; He, Z.; Jin, L.; Liu, G. Rheological, Mechanical, and Electrical Properties of Sr 0.7 Bi 0.2 TiO 3 Modified $BaTiO_3$ Ceramic and Its Composites. *Journal of the American Ceramic Society* **2023**, *106*, 3052–3065, doi:10.1111/jace.18997.
46. Nayak, S.; Venkateshwarlu, S.; Budisuharto, A.S.; Jørgensen, M.R.V.; Borkiewicz, O.; Beyer, K.A.; Pramanick, A. Effect of A-site Substitutions on Energy Storage Properties of $BaTiO_3$-$BiScO_3$ Weakly Coupled Relaxor Ferroelectrics. *Journal of the American Ceramic Society* **2019**, *102*, 5919–5933, doi:10.1111/jace.16449.
47. Cao, W.P.; Li, W.L.; Dai, X.F.; Zhang, T.D.; Sheng, J.; Hou, Y.F.; Fei, W.D. Large Electrocaloric Response and High Energy-Storage Properties over a Broad Temperature Range in Lead-Free NBT-ST Ceramics. *J Eur Ceram Soc* **2016**, *36*, 593–600, doi:10.1016/j.jeurceramsoc.2015.10.019.